JOURNAL OF ZANKOY SULAIMANI

Part -A- (Pure and Applied Sciences)

VOLUME 25 ISSUE 2 December 2023

ISSN: 1812-4100

www.jzs.univsul.edu.iq

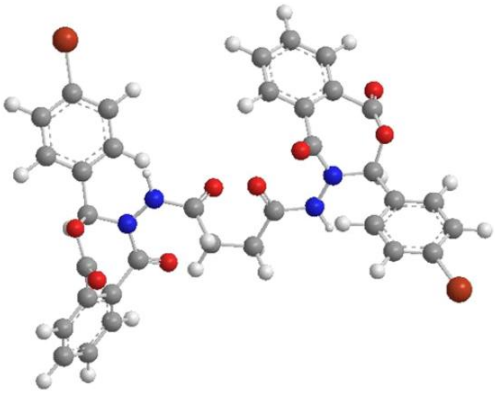

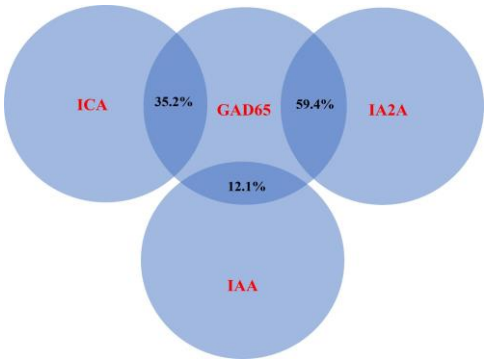

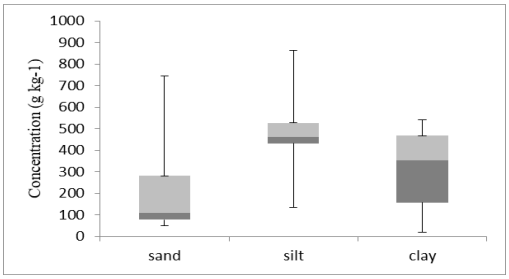

Journal homepage www.jzs.univsul.edu.iq
Journal of Zankoy Sulaimani
Part-A- (Pure and Applied Sciences)
ISSN:1812-4100

Trivalent Metal Complexes of Rich-Hyrdoxy Schiff base Ligand: Synthesis, Characterization, DFT Calculations and Antimicrobial Activity

Hanar Q. Hassan [1,*], Karzan A. Abdalkarim [1,*], Dalia A. Abdul [1], Aso H. Hasan [2], Diary I. Tofiq [1], Rebaz F. Hamarawf [1], Shujahadeen B. Aziz [3], Kawan F. Kayani [1]

1 *Department of Chemistry, College of Science, University of Sulaimani, Qliasan street, 46001 Sulaymaniyah, Kurdistan Region, Iraq*
2 *Department of Chemistry, College of Science, University of Garmian, Bardesur Street 46021, Kalar, Kurdistan Region, Iraq.*
3 *Research and Development Center, University of Sulaimani, Qliasan Street, 46001 Sulaymaniyah, Kurdistan Region, Iraq*
* Corresponding email: karzan.abdalkarim@univsul.edu.iq, hanar.hassan@univsul.edu.iq

Article info
Original: 4/7/2023
Revised: 29/7/2023
Accepted: 9/8/2023
Published online: 20/12/2023

Key Words:
4,4'-oxydianiline, hydroxy-rich, Schiff base, heteroatom, trivalent metal complex, DFT, antibacterial

Abstract

The design of trivalent metal complexes involves choosing suitable ligands that can bind to the metal and confer the desired properties. In this study, novel trivalent metal complexes (TVMCs) of Ru, Fe, and Cr were synthesized from a newly developed hydroxy-rich Schiff base ligand (LH_2) derived from 4,4'-oxydianiline with 2, 4-dihydroxybenzaldehyde, which is referred to as *N*, *N*`-bis [2,4-dihydroxyphenyl-methylidene] 4,4'-oxydianiline (LH_2). The ligand synthesis was performed using reflux without a catalyst in ethanol. The products underwent thorough characterization experimentally by various techniques such as: FT-IR, ^{1}H-NMR, ^{13}C-NMR, Powder XRD, elemental analysis, UV-Visible, conductivity, magnetic susceptibility, and thermal gravimetric analysis. The molar conductance measurements suggest that the complexes are non-electrolytes and do not contain conductive species outside the coordination sphere. Thus they can be formulated as $[MLCl(H_2O)].nH_2O$. Magnetic moment and electronic spectral studies confirmed that all complexes exhibit octahedral geometry around the metal ion. Furthermore, density functional theory (DFT) calculations were performed theoretically to investigate the structures, frontier molecular orbitals (HOMO and LUMO), molecular electrostatic potential (MEP), and electron localization function (ELF) for all complexes, utilizing the Gaussian09 software and the B3LYP/6-311+G(d, p) level. In vitro experiments were conducted to evaluate the antibacterial activity of the compounds against both Gram-negative (*Escherichia coli*) and Gram-positive (*Staphylococcus aureus*) bacterial species, using the agar diffusion method. The results indicate that the Fe(III)-complex exhibits noteworthy inhibitory effects on both Gram-positive and Gram-negative bacteria, with a maximum inhibition zone.

Introduction

Heteroatoms such as N and O in hydroxy-rich Schiff base ligands have received extensive investigation in the synthesis of trivalent metal complexes[1–3], owing to their unique coordination environments and potential applications in various fields. In recent years, Ru(III), Cr(III), and Fe(III) complexes with such ligands have attracted significant attention due to their diverse structures and enhanced stability and reactivity[4]. The presence of N and O heteroatoms in ligands enhance metal-ligand bonding and redox properties of hydroxy ligands, which are useful in catalysis, bioinorganic chemistry, and medicinal

chemistry. Nitrogen-containing ligands also provide diverse electronic and steric effects for metal centers, which are useful in sensors and luminescent materials. Trivalent metal complexes with hydroxy-rich ligands containing N and O heteroatoms have potential applications in these fields.[5–7].

The HSAB (Hard and Soft acids-bases) principle classifies metals and heteroatoms in ligands as hard or soft based on their electronegativity and atomic radius. This principle predicts the stability of metal-ligand complexes, where hard metals prefer hard heteroatoms and soft metals prefer soft heteroatoms. The HSAB principle also helps to design new ligands for specific metal ions, with applications in catalysis and drug discovery[8–10].

For the past ten years, researchers have focused their attention on macrocyclic Schiff base compounds containing azomethine groups, and their coordinated complexes have been extensively and consistently studied due to their wide range of applications in areas such as epoxy resin organic coating[11], anticorrosive coating materials[12], catalysis for Ring-Opening Polymerization[13–15], degradation of toxic dyes[16], cytotoxicity[17], antimicrobial[18], and antibacterial activities[19]. Diamine starting materials, 4,4-diamino diphenyl ether, also known as 4,4-oxydianilline, have two primary amines with a chemical formula of $C_{12}H_{12}N_2O$. This primary amine can be modified and used in the biological and medical fields[19]. Different types of Schiff bases can be synthesized by condensing 4,4-diamino diphenyl ether with various compounds, such as o-vanillin[20,21], salicylaldehyde[22–24], and phthalaldehyde[25]. Additionally, chelation with suitable metal ions enhances the biological efficacy and improves the stability of Schiff base complexes, and their size and morphology offer suitable opportunities for extensive investigation and application in various industrial and medical fields[25]. Metal ions, such as ruthenium, chromium, or iron, and their complexes have shown promising biological activity, such as antitumor[26], antibacterial [27], and anticancer[28,29]. In addition to the well-known chromium complexes, iron and ruthenium have recently been identified as potential substitutes for use as homogeneous catalysts[30].

Different studies have reported that several compounds containing (LH_2) moiety possess anti-mycobacterial activity, which may be useful in developing new and potent anti-mycobacterial agents[31], exhibit urease inhibitory activity[32], show significant catechol oxidase activity[33], and display catalytic activities[34]. Additionally, polydentate (LH_2) compounds are appealing ligands for the creation of polynuclear manganese clusters, which are produced by condensation of 2-hydroxybenzaldehyde or its derivatives with a variety of amino alcohols[35].

To understand the structure, stability, and reactivity of these complexes, density functional theory (DFT) calculations are often employed as a powerful computational tool. DFT is a computational tool that can reveal the electronic and geometrical features of metal complexes with hydroxy-rich Schiff base ligands, as well as their molecular orbitals, electrostatic potential, and electron localization function. DFT can also help to design new ligands based on the hard and soft acids and bases concept, and predict the biological properties of the complexes based on the energy gap between the HOMO and LUMO. DFT is a useful method for studying these complexes[36,–39].

In this report, a symmetrical Schiff base ligand was synthesized from the condensation reaction of 4,4'-oxydianiline with 2,4-dihydroxybenzaldehyde to form (LH_2). It is designed to strongly bind trivalent metal ions, such as Ru(III), Fe(III), and Cr(III). **Figure 1** represents the main aspects and a graphical summary of this work.

The Experimental Part

Materials

All metal (III) chloride salts, ethanol, methanol, and 2,4-dihydroxy benzaldehyde were purchased from Merck Company. The chemicals 4,4'-oxydianiline, DMSO, THF, and diethyl ether were supplied by Solarbio, Fisher Scientific, Alfa Chemika, and Biochem companies respectively. The chemicals were all analytically pure, therefore no further Varian INOVA machine at frequencies of 500MHz for ^{1}H-NMR and 126MHz for ^{13}C-NMR in DMSO d^6 at 25 degrees Celsius purification was required.

Characterization techniques

The experiment utilized various equipment and instruments to analyze the compound. Thin Layer Chromatography (TLC) was performed on a precoated silica gel plate. Melting points were determined using an electro-thermal digital melting point machine with open glass capillary tubes. The compound (LH_2) was analyzed using a. The IR spectra of (LH_2) and its (TVMC)s were recorded on KBr pellets in the range of 400-4000 cm^{-1} using a Perkin-Elmer FTIR spectrophotometer. The compound's elemental composition of C, H, and N was determined using the Eurovector EA3000 series analyzer, and the magnetic susceptibility of the complexes was measured at 20 degrees Celsius using the Sherwood Scientific Auto Guoy balance instrument. Powder X-ray diffraction (PXRD) was performed using a PANalytical X'Pert Pro X-Ray Diffraction Spectrometer diffractometer. The molar conductance of the complexes in DMSO was measured using a Fisher Scientific Multimeter Model XL600. The electronic transitions of (LH_2) and (TVMC)s in DMSO solutions were determined using a Cary Eclipse UV-Visible Spectrophotometer from Agilent Technologies in the wavelength range of 250-750 nm. Lastly, thermal gravimetric analysis (TGA) was conducted on the Perkin Elmer Diamond TGA/DTA (SII) thermal analyzer in an air atmosphere with a heating rate of 10 degrees Celsius per minute.

DFT Calculations

The Gaussian09 software was used to perform density functional theory (DFT) calculations[40]. To optimize the different complexes, we applied the most accurate and reasonable functional B3LYP and LANL2DZ/6-311G(d,p) basis set *via* DFT[41–43]. The LANL2DZ basis set was limited to core potential metals Cr(III), Fe(III), and Ru(III), and the 6-311G(d,p) basis set involved one set of d and p functions to describe the molecular and electronic properties of organic molecules (C, H, N, O, and Cl) [44]–[48]. The calculations were carried out in the gas phase. The selected basis set was primarily chosen to the effective calculation of core potentials for post-third-row atoms. Geometrical parameters were generated to study the coordination structural environment around the metal atoms. The Chemcraft[49] and GaussView [50] programs were used to visualize the structural optimization, perform some calculations, and analyze frontier molecular orbitals (FMOs). To compare the vibrational data with experimental results [45, 51, 52], the 6-311G(d,p) harmonic vibrational modes were scaled by a factor of 0.967 for light atomic systems (organic molecules)[53]. The LANL2DZ fundamental harmonic vibrations (responsible for heavy metals Cr, Fe, and Ru) were scaled by a factor of 0.961. The electron localization function (ELF) was studied with the aid of the Multiwfn software[54] to investigate the electron-localized regions on the surface of coordinated complexes.

Synthesis of Schiff base (LH_2)

To synthesize the Schiff base Ligand (LH_2), a mixture of 4,4'-oxydianiline (0.5 g, 2.5 mmol) and 2,4-dihydroxy benzaldehyde (0.69 g, 5.0 mmol) was heated under reflux in 10 mL of ethanol with constant stirring for 8 hours. The completion of the reaction was monitored by TLC using n-hexane-ethyl acetate (1:1). The solvent was then removed under reduced pressure via rotary evaporation and the reaction mixture

was cooled to room temperature. The crude solid residue was recrystallized to obtain a pure Schiff base with a 75% yield.

General method for the synthesis of Cr(III), Fe(III), and Ru(III) complexes

(TVMC)s of (LH_2) were synthesized by adding dropwise 10 mL of THF solution (0.34 mmol, 0.097g, 0.137g and 0.136g respectively) of $RuCl_3.3H_2O$, $Fe(NO_3)_3.9H_2O$, and $Cr(NO_3)_3.9H_2O$ to the constantly stirring solutions of the prepared Schiff base (0.34 mmol) in 20 mL of THF. The mixtures were refluxed for 24 hrs. A precipitate formed, which was then filtered and washed several times with distilled water, THF, and diethyl ether. All complexes were dried under vacuum at room temperature.

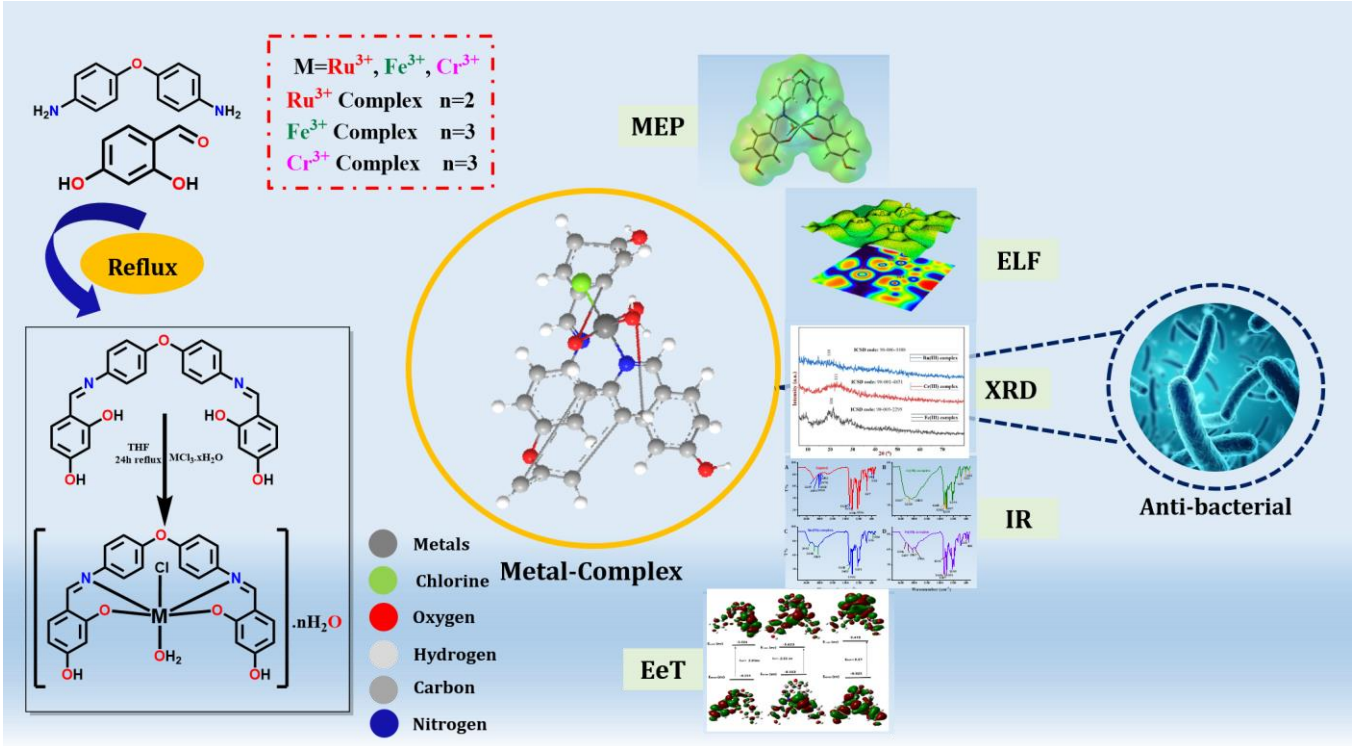

Figure 1: Schematic representation of complex formation, characterization, and application with proposed structure of (LH_2) and its (TVMC)s

Antibacterial activity

The antibacterial activity of a newly synthesized Schiff base, its trivalent metal chelates, and a standard antibiotic (Cefotaxime, CTX-30) was assessed using the agar diffusion method with Muller Hinton agar medium[55]. Two clinical strains of bacteria, *Escherichia coli* and *Staphylococcus aureus*, were selected as the test organisms because they are common pathogens in hospital settings. These strains were obtained from culture-based techniques of samples collected from infected patients and were identified by the VITEK® 2 system and biochemical tests. For the agar diffusion assay, the bacterial culture was uniformly swabbed on the agar plate, and wells were made in the agar medium. The wells were filled with 40µL of test solutions, which were prepared by dissolving 20mg/mL of the compounds in DMSO. For comparison purposes, DMSO and Cefotaxime (CTX-30) were used as the controls for the solvent and standard compound, respectively. After incubating the plates for 24 hrs at 37°C in an incubator, the diameter of the inhibition zone in millimeters around each well was measured to determine and compare the antibacterial activity of each sample with the standard drug.

Results and discussion

The Schiff base (LH_2) was synthesized by the reaction of 4,4'-oxydianiline and two moles of 2,4-hydroxy benzaldehyde, using Reflux method, as shown in **Figure 1**. Additionally, all TVMCs with ruthenium, chromium, and iron were obtained under the same reaction conditions. These air-stable-colored powders are easily soluble in polar solvents such as DMSO, DMF, and methanol but insoluble in diethyl ether and THF. Physical properties, analytical data, magnetic moments, and molar conductance value of the compounds agreed well with the suggested formulation. The elemental C, H, and N analyses of (LH_2) and its (TVMC)s showed good agreement between the calculated and experimental values, which supported the stated formulas displayed in **Table 1**. Furthermore, the elemental analysis indicated that the coordination of the Schiff base to metal ions was 1:1 on a mole basis, indicating that one mole of the LH_2 reacted with one mole of metal salt.

Table 1: Physical properties and elemental analysis for (LH_2) and their (TVMC)s.

Compound	M.wt	Color	Yield%	M.P °C	% Found (Calculated)		
					C	H	N
Ligand (LH_2)	440.46	Yellow	75	234	70.87 (70.90)	4.53(4.58)	6.33 (6.36)
[Ru(L)(Cl)(H_2O)].2H_2O	629	Black	84	>323	48.75 (49.65)	3.73(3.85)	4.39 (4.45)
[Fe(L)(Cl)(H_2O)].3H_2O	601.79	Brown	76	>300	52.18 (51.89)	4.56(4.35)	4.83 (4.66)
[Cr(L)(Cl)(H_2O)].3H_2O	597.95	Brown	71	>377	53.10 (52.23)	4.57(4.38)	4.80 (4.69)

FT-IR Spectra

The FTIR frequencies of related functional groups of the Schiff base and its (TVMC)s, along with their assignments are given in **Table 2**, and the FT-IR spectra of the ligand and its (TVMC)s are shown in **Figure 2**. The appearance of the (CH=N) imine stretching band at 1630 cm^{-1} for (LH_2)[56], which was absent from the precursor amine reactant, indicates the synthesis of the ligand. This is further supported by the absence of the NH_2 stretching band in the IR spectrum of the (LH_2) (**Figure 2**).

Another indication that the ligand was formed is the emergence of bands responsible for the aliphatic C-H stretching of the alkene and imine group (H-C=N) at (2893-2978 cm^{-1})[57], whereas the aromatic (C-H) stretching is observed at frequencies between (3032-3098 cm^{-1}). Furthermore, a band at 1612 cm^{-1} is assigned to (C-N) frequency[58]. The band observed at 1496 cm^{-1} indicates the presence of the (C=C) functional group in the (LH_2) ligand[57].

Table 2: Selected FT-IR spectral data of (LH_2) and its (TVMC)s.

Compound	O-H	O-H (H_2O)	$C_{(Ar)}$-O	CH=N	N-C	M-N	M-O	M-Cl
Ligand (LH_2)	3237	-	1256	1630	1612	-	-	-
[Ru(L)(Cl)(H_2O)].2H_2O	3240	3445	1241	1638	1603	490	536	458
[Fe(L)(Cl)(H_2O)].3H_2O	3237	3346	1240	1606	1597	488	529	419
[Cr(L)(Cl)(H_2O)].3H_2O	3238	3367	1244	1608	1583	484	555	456

The metal-ligand bonding can be determined by comparing the IR spectra of the Schiff base ligand and its complexes. The ligand is a hydroxy-rich compound with four (O-H) groups. In the IR spectra of (LH_2) and its (TVMC)s, the weak and broad bands in the range of (3237-3240 cm^{-1}) are attributed to uncoordinated (O-H) groups of phenols[59, 60], while the weak and broad bands located at (3346-3445 cm^{-1}) in the spectra of complexes are assigned to either hydrated or coordinated water molecules[61]. Another band related to the

phenolic groups is (C-O), which is present at 1256 cm^{-1} in the ligand[61, 62] and shifts to a lower frequency in all (TVMC)s to (1240-1244 cm^{-1}). This is a strong indication that coordination between two phenolic groups of the (LH_2) with metals was involved[48, 49].

The results of the IR spectra and elemental analysis indicate that (M-O) bond formation has occurred with some hydroxy groups, while some other hydroxy groups remain uncoordinated. Even though the (M-O) bond exhibits weak bands at (529-555 cm^{-1}), which are attributed to the coordination of phenolic and/or water molecules to the metal ions[57], it is not clear which specific hydroxy groups are involved in the metal coordination.

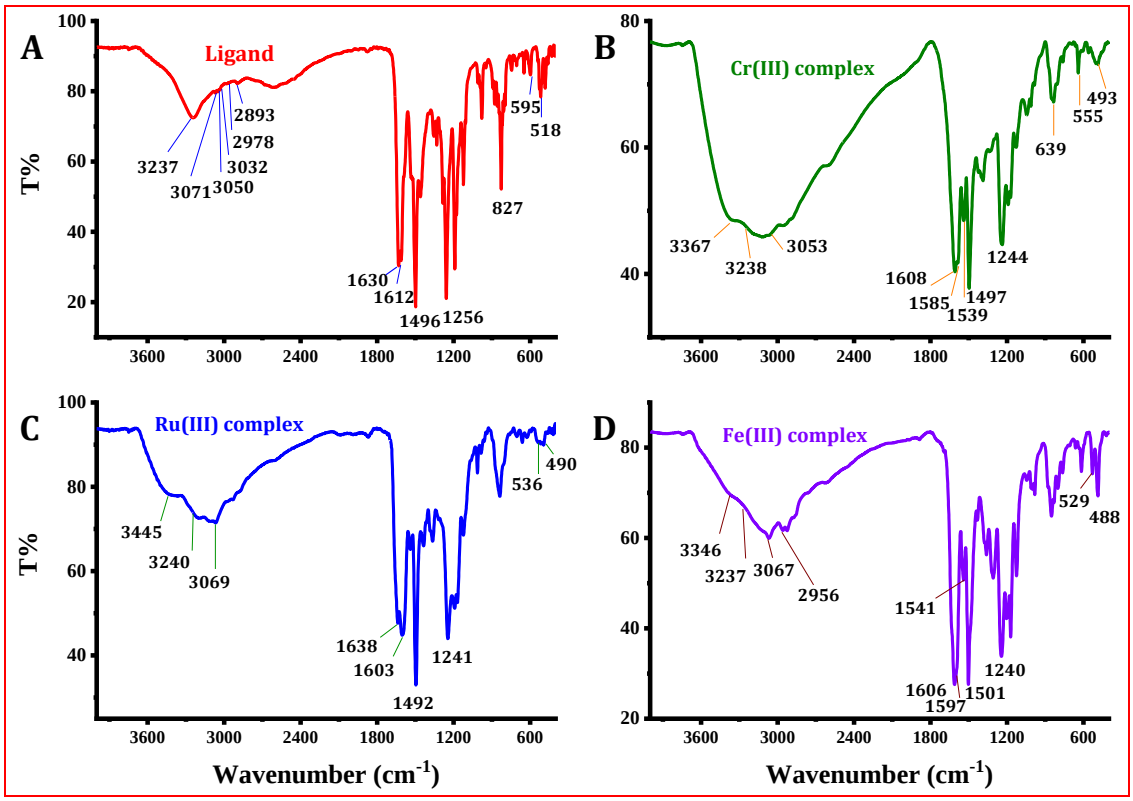

Figure 2: FT-IR Spectra of the Schiff base ligand and its (TVMC)s.

The IR spectrum of (LH_2) and its (TVMC)s shown in **Figure 2** demonstrates that the azomethine band (CH=N) shifted to a lower frequency in the IR spectra of all complexes except for Ru(III) complex, which shifted to a higher frequency. The shift in the original band position by (8-24 cm^{-1}) confirms the involvement of nitrogen in coordination with metal ions. Additionally, the bands centered at (484-490 cm^{-1}) in the spectra of all complexes confirm (M-N) bond formation[63]. Weak bands with low intensity at (419-458 cm^{-1}) are present in the spectra of all complexes, which further supports the formation of (M-Cl) within the complexes and provides evidence for their successful formation[55]. The similarity in the shape and location of the absorption bands, which is due to using the identical ligand for all complexes and using metal ions of the same nature and properties, suggests similar coordination modes for the complexes.

^{1}H-NMR and ^{13}C-NMR spectral studies

The ^{1}H-NMR and ^{13}C-NMR of the Schiff base were recorded at room temperature (*r.t.*) in DMSO-d^{6} representing the chemical shifts of different positions of protons and carbons which confirm the formation of (LH_2).

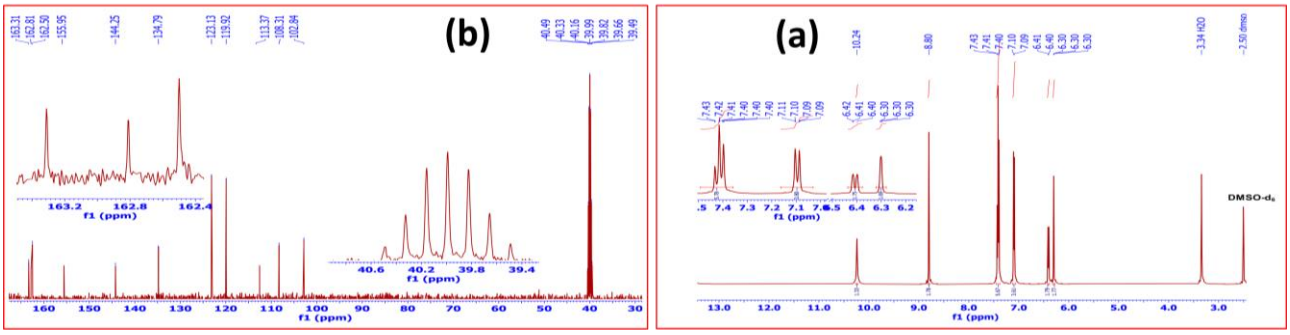

Figure 3: (a) ^{1}H-NMR and (b) ^{13}C-NMR Spectra of (LH_2).

Based on the positions of its atoms, the numbering of the structure of (LH_2) is shown in **Table 3**. In the ^{1}H-NMR spectrum of the ligand in **Figure 3(a)**, two sharp singlet peaks at (10.24 and 13.51 ppm) were attributed to both hydroxy groups numbered 7 and 8 [59]. The band of O-H8 was shifted downfield (magnitude of due to intramolecular hydrogen bonding between it and the nitrogen of imine (OH---N=C)[63]. Furthermore, peaks at (6.30, 6.40, 6.41, 7.09, 7.10, 7.40, 7.41, and 7.43 ppm) indicated aromatic hydrogens on carbons (1-5) as (C4-H(s), C1-H(d), C2-H(d), C5,3-H(s)(d)) respectively. Another peak at (8.80 ppm) confirmed the formation of the (H-C=N) of the azomethine group of the (LH_2)[30][59].

The ^{13}C-NMR spectrum of (LH_2) in **Figure 3(b)** showed two peaks at (162.81 and 163.31 ppm) attributed to the carbons of the aromatic cycle in the type of (C-O-H)[30] and the imine group (CH=N) showed a peak for its carbon at (113.37 ppm)[30, 64]. Additional peaks in various positions on the spectrum were attributed to other aromatic carbons in diverse environments, as shown by the (LH_2) structure in **Table 3** and their corresponding numbers. However, NMR techniques were not performed for the complexes because they are all paramagnetic[65].

UV–Visible spectra

Table 4 presents the electronic spectral data of (LH_2) and its (TVMC)s in DMSO. **Figure 4** shows the UV-vis spectra spectrum of (LH_2), which exhibit an absorbance band at 290 nm on the higher energy side, corresponding to the n→$\pi*$ transition of the ethereal oxygen of (LH_2). In addition, another peak is observed at 354 nm, attributable to the n→$\pi*$ transitions of the imine groups[59]. The appearance of newly observed peaks in the shorter wavelength region and the shift in the absorption bands of the complexes compared to those of (LH_2) confirm the formation of complexes between the metal ions and (LH_2)[55].

Table 3: ^{1}H-NMR and ^{13}C-NMR spectral data of (LH_2).

^{1}H-NMR	**Assignment**	**Chemical shift (δppm)**
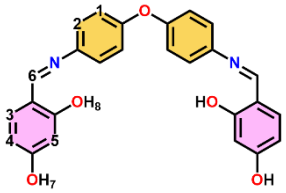	hydrated water molecule	3.34
	C4-H(s),C1-H(d), C2-H(d),C5,3-H(s)(d)	6.30,6.40, 6.41, 7.09, 7.10, 7.40, 7.41, 7.43,
	C6-H (s)	8.80
	OH7 (s)	10.24
	OH8 (s)	13.51
^{13}C-NMR	**Assignment**	**Chemical shift (δppm)**
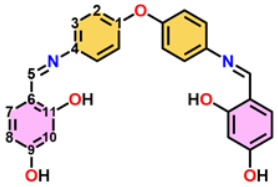	C10, C8	102.84, 108.31
	C3, C2, C6	123.13, 119.92, 113.37
	C1, C4, C7	155.95, 144.25, 134.79
	C11, C9, C5	163.31, 162.81, 162.50

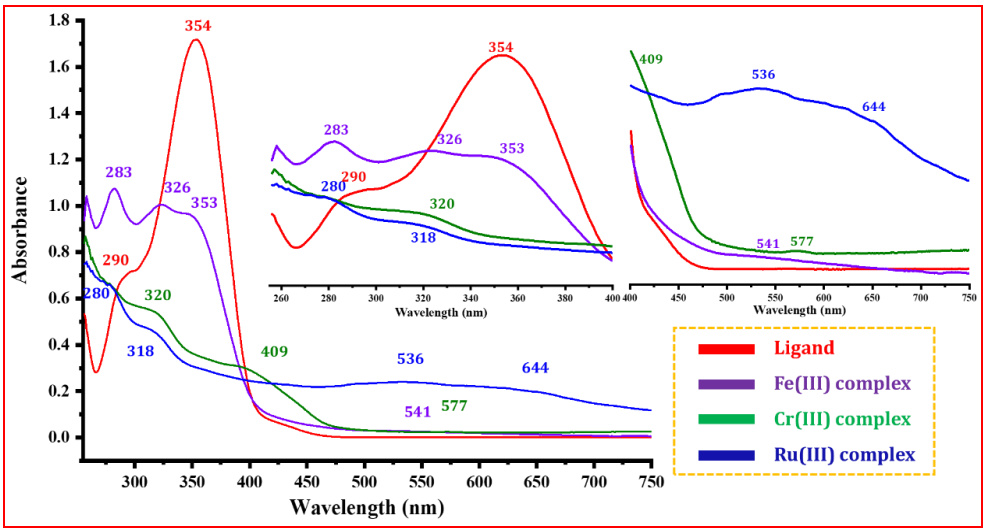

Figure 4: UV-Visible spectra of (LH_2) and its (TVMC)s in DMSO solvent.

The electronic spectrum of the Cr(III) complex revealed two bands at 577 nm and 600 nm, due to the $^{4}A_2g(F)\rightarrow{}^{4}T_1g(F)$ transition, in an octahedral geometry, whereas the third band is within the range of (LH_2) transitions anticipated for the complex at 409 nm. This band is caused by the $^{4}A_2g(F)\rightarrow{}^{4}T_1g(P)$ transition[27, 66].

The electronic spectrum of the Ru(III) complex shows absorption bands at (371 nm, 536 nm, and 644 nm) which can be attributed to $^{2}T_2g\rightarrow{}^{4}A_1g$, $^{2}T_2g\rightarrow{}^{4}T_2g$, and $^{2}T_2g\rightarrow{}^{4}T_1g$ transitions in the order of decreasing energy. The position of the bands in tune suggests that Ru(III) is surrounded by an octahedral environment[66, 67].

In the spectrum of the Fe(III) complex, it can be seen that it exhibits two bands at 541 nm and 434 nm, which can be assigned to the $^{6}A_1g\rightarrow{}^{4}T_1g$ and $^{6}T_2g\rightarrow{}^{5}Eg$ transitions, respectively. These transitions are indicative of an octahedral geometry[30, 68, 69].

Table 4: UV-visible, magnetic susceptibility, and molar conductance of (LH_2) and their (TVMC)s.

Compounds	Absorption Band (nm)	Assignments	μ_{eff} (B.M.)	Λ_m (S^{-1} cm^2 mol^{-1})
Ligand (LH_2)	255, 290, 354	$\pi \rightarrow \pi^*$, n $\rightarrow \pi^*$	-	-
$[Ru(L)(Cl)(H_2O)].2H_2O$	257, 280, 318 371 536 644	$\pi \rightarrow \pi^*$, n $\rightarrow \pi^*$ $^2T_2g \rightarrow {}^4A_1g$ $^2T_2g \rightarrow {}^4T_2g$, $^2T_2g \rightarrow {}^4T_1g$	1.78	16.142
$[Fe(L)(Cl)(H_2O)].3H_2O$	258, 285, 326 434 541	$\pi \rightarrow \pi*$, n $\rightarrow \pi*$ $^6T_2g \rightarrow {}^5Eg$ $^6A_1g \rightarrow {}^4T1g$	5.62	26.612
$[Cr(L)(Cl)(H_2O)].3H_2O$	258, 320 409 577 600	$\pi \rightarrow \pi*$, n $\rightarrow \pi*$ $^4A_2g(F) \rightarrow {}^4T_1g(P)$ $^4A_2g(F) \rightarrow {}^4T_1g(F)$ $^4A_2g(F) \rightarrow {}^4T_2g(F)$	3.93	24.832

Magnetic moment

Table 4 presents the magnetic moments of the (TVMC)s at (*r.t.*). The Cr(III) complex exhibits a magnetic moment of 3.93 B.M, indicating the presence of three unpaired electrons in its outer valence shell[27, 55]. The measured value of 1.78 B.M suggests that the Ru(III) complex is a low spin d^5 complex with one unpaired electron[66, 67, 70]. The recorded value of 5.62 B.M suggests that the Fe(III) ions in the complex possess high spin and have five unpaired electrons in their outer valence shell[27, 69]. Additionally, all complexes exhibit octahedral geometry.

Molar conductance

The molar conductance of (10^{-3} M) of the prepared complexes in DMSO solution at (*r.t.*) is listed in **Table 4**. Based on the molar conductance values, a range of 16 to 27 $S.cm^2.mol^{-1}$ for the complexes was obtained. The observed low conductivities of the (TVMC)s suggest that they are non-electrolytic in nature[62], which is consistent with the coordination of chloride ions with the metal ions in the complexes. To further confirm the non-electrolytic nature of the complexes, $AgNO_3$ was added to the solutions of the metal complexes, and no white precipitate was formed, indicating that the chloride ions are not located outside the coordination sphere as accompanying ions[55]. This experimental evidence supports the proposed geometry of the complexes.

Powder XRD

X-ray powder diffraction (XRD) was used to investigate the structural properties of the (LH_2) and its metal complexes. The XRD patterns are shown in **Figure 5**. The Schiff base ligand (LH_2) showed sharp peaks at 2θ values of 14.52°, 18.15°, 19.82° and 24.53°, confirming its crystalline nature. The average crystalline size (d) of the LH_2 ligand was calculated to be 25.82 nm using Scherrer's formula[71]. The metal complexes of LH_2 with Fe(III), Cr(III) and Ru(III) displayed broad peaks at 2θ values of 20.07°, 22.19° and 18.70°, respectively, indicating their amorphous nature. This could be attributed to the coordination of the metal ions to the ligand, which may affect the regular packing of the ligand molecules and cause a loss of crystallinity.

The broadening of the peaks in all complexes also suggests that the Schiff base undergoes quantum confinement in the chelates due to the attachment of donor atoms to metal ions[72, 73].

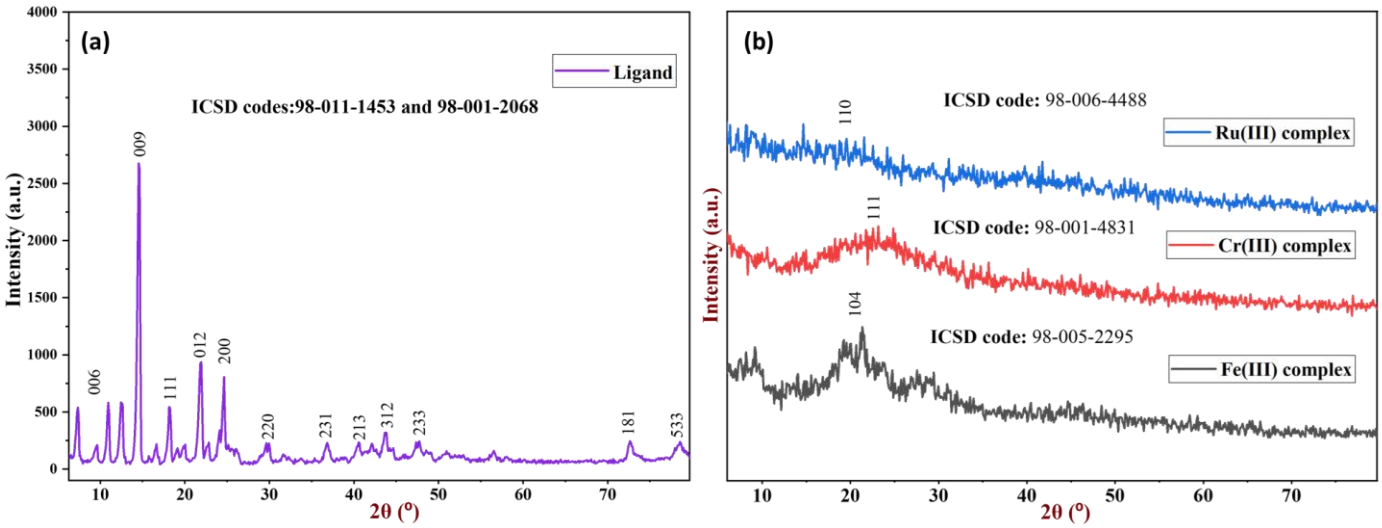

Figure 5: X-ray diffraction patterns of (a) ligand and (b)its complexes.

Thermal analysis

The thermal stability of the (TVMC)s was evaluated by performing TGA within a temperature range of 30 to 600°C, using a linear heating rate of 10°C/min under an air atmosphere. The thermograms presented in **Figure 6** were analyzed to extract the thermal data of the decomposition steps, which are listed in **Table 5**.

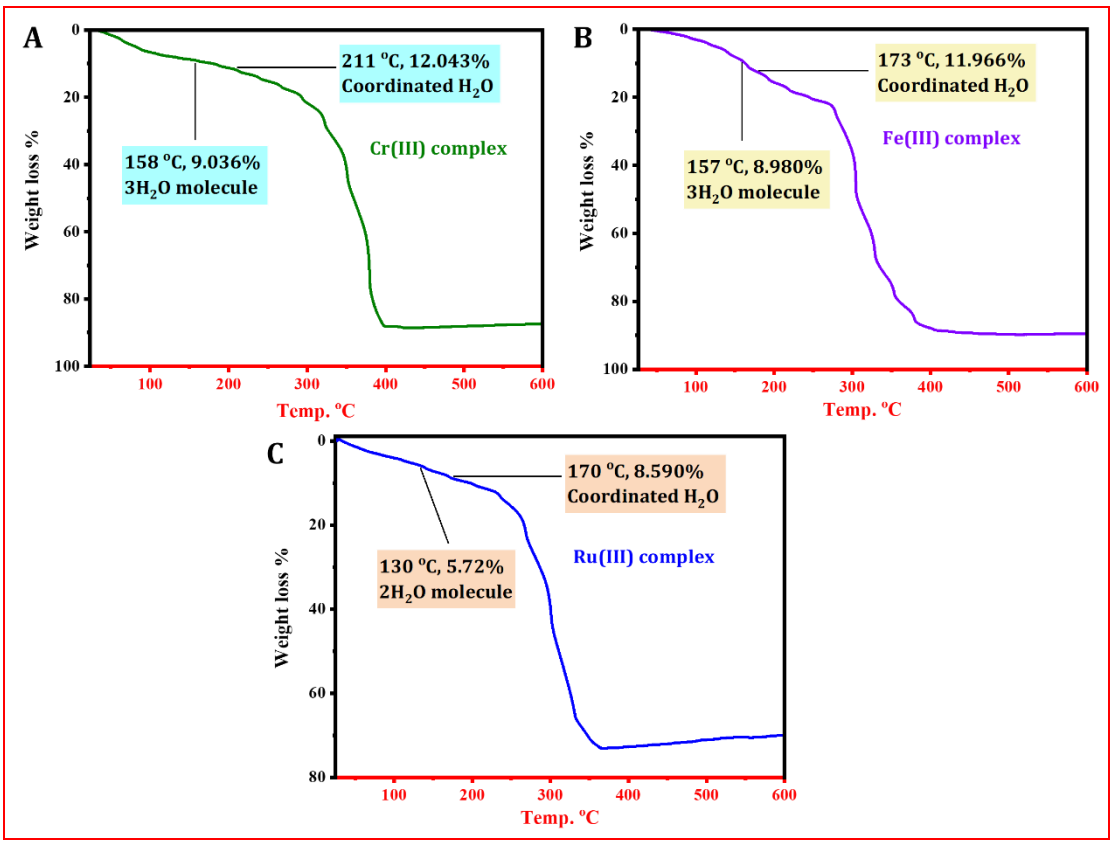

Figure 6: Thermograms (TVMC)s of Cr(III), Fe(III), and Ru(III).

Thermogravimetric analysis (TGA) can be used to determine whether water molecules are located in the inner or outer coordination sphere of a complex. Hydrated water molecules are eliminated at temperatures below 160°C while coordinated water molecules are rejected between 160 and 250°C[57]. The thermograms showed that all complexes followed the same pattern of decomposition which involves the removal of moisture, dehydration of coordinated water molecules, dichlorination, and ultimately the breakdown of the organic moiety of the complexes. The chelate ligands of the complexes are thermally more stable than non-chelating ligands because the strength and chelation of the ligand have a significant impact on the order of thermal disintegration of complex fragments[74].

The complexes exhibit a thermal stability of about 130-158°C, which maintains their coordination sphere at a steady opposite with the increasing temperature. The first step of elimination involves the hydrated water molecules of all complexes. Three hydrated water molecules were removed for the Fe(III) and Cr(III) complexes at 157°C (8.980%) and 158°C (9.031%), respectively, while two hydrated water molecules were removed at 130°C (5.722%) for the Ru(III) complex. Additionally, one coordinated water molecule began to be lost at 170°C (8.590%), 173°C (11.966%), and 211°C (12.043%) for the Ru(III), Fe(III), and Cr(III) complexes, respectively, at different temperatures, followed by the loss of coordinated chloride ions and ultimately the organic moieties, based on their corresponding data shown in **Table 5**. Finally, the metal oxides remaining as residues, as mentioned in the table for all complexes, provide additional confirmation of the proposed structure of the complexes shown in **Figure 1**.

Ultimately, the thermal stability of the (TVMC)s was evaluated using TGA, which showed that the complexes could withstand temperatures up to 130-158°C. The decomposition of the complexes involved several steps, including the removal of moisture, dehydration of coordinated water molecules, dichlorination, and breakdown of the organic moiety. The thermal stability of the chelate ligands was higher than that of non-chelating ligands due to the strength and chelation of the ligand. The complexes contained both hydrated and coordinated water molecules that were eliminated at different temperatures. The metal oxides remaining after decomposition confirmed the proposed structure of the complexes. These results provide important information about the thermal stability and decomposition pathways of the complexes, which could help in the development of new metal-based compounds with improved properties.

Table 5: Thermal analysis data of (TVMC)s.

Compounds	TG range ºC	Mass Loss%	Compound decomposition	Residue%	Metallic residue
		Calc. (est.)		Calc. (est.)	
[Ru(L)(Cl)(H_2O)].2H_2O	33-130	5.723 (5.722)	2H_2O^h	19.883 (20.567)	½ Ru_2O_3
	130-170	8.585 (8.590)	H_2O^c		
	170-241	14.220 (14.231)	Cl^-		
	241-315	52.694 (52.702)	$C_{14}H_{10}O_4$		
[Fe(L)(Cl)(H_2O)].3H_2O	37-157	8.973 (8.980)	3H_2O^h	13.268 (13.513)	½ Fe_2O_3
	157-173	11.964 (11.966)	H_2O^c		
	173-219	17.855 (17.858)	Cl^-		
	219-321	58.069 (58.109)	$C_{14}H_{10}O_4$		
[Cr(L)(Cl)(H_2O)].3H_2O	30-158	9.031 (9.032)	3H_2O^h	12.709 (12.596)	½ Cr_2O_3
	158-211	12.041 (12.043)	H_2O^c		
	211-277	17.970 (17.975)	Cl^-		
	277-371	58.443 (58.453)	$C_{14}H_{10}O_4$		

H_2O^h is hydrated water molecule and H_2O^c is coordinated water molecule

DFT calculations

Geometry optimization

Some geometrical properties of (TVMC)s can be interpreted through the bond lengths and bond angles as presented in **Table 6** between the metal center and (LH_2) active sites. **Figure 7** shows the optimized structures of the Cr-complex, Fe-complex, and Ru-complex, which adopted the geometrical configuration of a distorted octahedral. The chelating (LH_2) (tetradentate) has a principal role in this distortion as N_1-Cr-N_2 and O_2-Cr-O_3 angles take the values 118.610° and 81.028° respectively, the same trend in the angle values of Fe(III) and Ru(III) complexes.

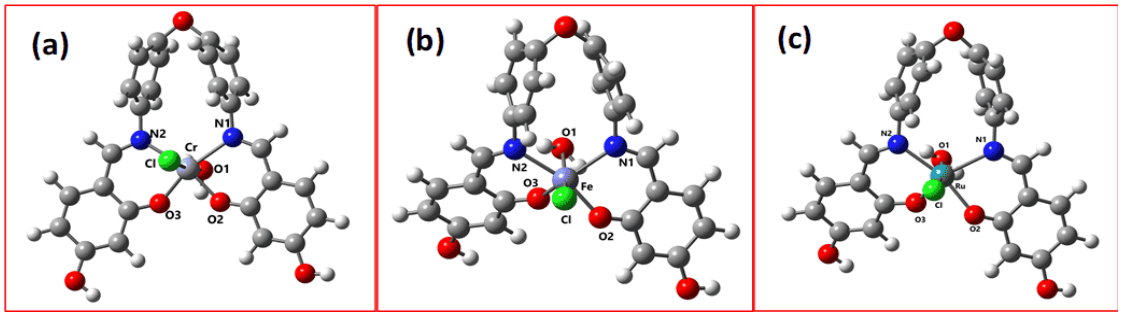

Figure 7: Optimized geometry for (TVMC)s of (a) Cr(III), (b) Fe(III), and (c) Ru(III)

Table 6: Selected bond lengths (Å) and bond angles (°) of the studied complexes at B3LYP/ 6–311 G(d,p) in gas

Bond Length (Å)	Cr-complex	Fe-complex	Ru-complex
M-O_1	2.226	2.365	2.317
M-O_2	1.901	1.912	2.069
M-O_3	1.963	1.885	1.988
M-Cl	2.410	2.330	2.257
M-N_1	2.261	2.176	2.280
M-N_2	2.156	2.163	2.202
Bond Angle (°)	**Cr-complex**	**Fe-complex**	**Ru-complex**
O_1-M-O_2	100.366	93.971	102.240
O_1-M-O_3	80.448	70.873	63.476
O_1-M-Cl	164.052	164.857	170.237
O_1-M-N_1	84.243	74.321	82.642
O_1-M-N_2	97.179	79.065	82.571
O_2-M-O_3	81.028	83.802	81.900
O_2-M-Cl	69.097	89.595	85.269
O_2-M-N_1	77.707	83.674	78.926
O_2-M-N_2	157.254	163.927	164.556
O_3-M-Cl	108.618	128.579	112.140
O_3-M-N_1	151.021	128.519	136.151
O_3-M-N_2	87.770	84.0621	87.338
N_1-M-Cl	81.824	101.014	105.134
N_1-M-N_2	118.610	112.195	116.404
N_2-M-Cl	96.283	89.762	88.594

This variation in the angle plane is attributed to the chelating nature of (LH_2), where the N-atoms are restricted (not flexible in movement) due to the two phenyl groups connected with the O-atom as a bridge. This is also the case in the other complexes with variable coordination environments resulting in different angle values between them. Comparing the bond lengths between the studied complexes shows variation in their values due to the variable strength of interaction between the metal and donor sites. According to the crystal field theory, the elongated axial bond is attributed to the highly distorted environment around the complex. Therefore, when comparing the bond lengths of M-O_1 of water, it is noticed that the bond length is longer in the Fe-complex (2.365 Å) followed by the Ru-complex (2.317 Å) and smaller in the Cr-complex (2.226 Å).

Quantum chemical reactivity parameters

Most scientific fields that deal with interactive systems can be explained through significant quantum reactivity indices, which also affect biological activity[75]. FMO energy values can be used to generate physicochemical and reactivity parameters, providing insights into the electronic properties and stability of the studied complexes. Electronegativity (χ), ionization potential (IP), electron affinity (EA), chemical potential (μ), chemical hardness (η), and global softness (S) are the most effective parameters for describing molecular properties and are listed in **Table 7**. Increasing the HOMO-LUMO gap (EGAP, ΔE) leads to a more stable molecular system, which is a well-known fact. IP and EA are reversible parameters, with more electrophilic systems having a higher electron affinity and lower ionization potential. The Fe-complex, for instance, has a slightly higher EA and lower IP than the other complexes. Global softness characterizes the resistance to electron distribution change, with smaller S and higher η predicting a less polarizable molecular system, resulting in less stabilization in the solvent, as seen in the Fe-complex. The small ΔE of this complex confirms its higher kinetic stability, but it has a higher thermodynamic reactivity than the other studied complexes.

Table 7: Molecular electronic/reactivity parameters of the studied (TVMC)s [energy unit (eV)].

Compounds	E_{HOMO}	E_{LUMO}	ΔE	IP	EA	X	μ	η	S
Cr-complex	-8.354	-5.524	2.83	8.354	5.524	6.939	-6.939	1.415	0.353
Fe-complex	-8.163	-5.633	2.53	8.163	5.633	6.898	-6.898	1.265	0.395
Ru-complex	-8.925	-5.415	3.51	8.925	5.415	7.170	-7.170	1.755	0.285

The quantum chemical parameters are calculated from the following equations [76]:

$$\Delta E = E_{LUMO} - E_{HOMO} \quad (1)$$

$$\chi = (-(E_{HOMO} + E_{LUMO}))/2 \quad (2)$$

$$\eta = (E_{LUMO} - E_{HOMO})/2 \quad (3)$$

$$\mu = -\chi \quad (4)$$

$$S = 1/2\eta \quad (5)$$

$$\omega = \mu^2/2\eta \quad (6)$$

$$IP = - E_{HOMO} \quad (7)$$

$$EA = - E_{LUMO} \quad (8)$$

Frontier Molecular Orbitals (FMOs) analysis

The electronic transitions can be explained through the analysis of FMOs, as shown in **Figure 8**. Identifying the energy of transition states enables us to predict how the contribution of electronic molecular orbitals affects the formation of stable complexes. For example, in the case of the Cr-complex, the HOMO level contributes mostly to the presence of electrons around the donor centers, particularly N-donor atoms, and the electronic distribution is concentrated on the left side of the molecule. The LUMO state reverses the electronic distribution, with higher electronic excitation on the right side and an energy gap of 2.83eV. In the Fe-complex, the lowest energetic orbital is distributed around the donor (LH_2) center, and the distribution increases in the LUMO state, with an energy separation of 2.53eV. In the Ru-complex, the HOMO state has an electronic density distributed throughout the molecule, and this is the same for the highest energetic transition state, with an energy difference of 3.51eV. FMOs for these complexes reveal large electronic distribution scales, leading to the formation of highly stable complexes.

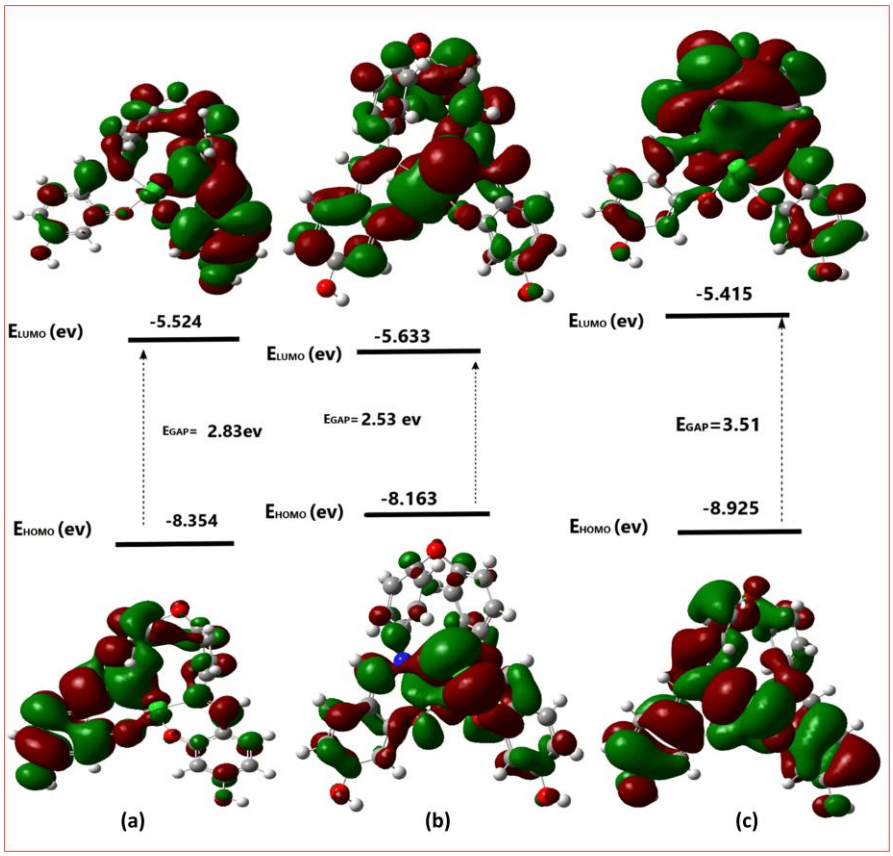

Figure 8: Energetic electronic transitions related to FMOs of the (TVMC)s of (a) Cr(III), (b) Fe(III), and (c) Ru(III)

Molecular electrostatic potential (MEP) analysis

MEP analysis is a suitable method to interpret the reactive sites on a complex surface. The color key, illustrated in **Figure 9**, is responsible for electrophilic and nucleophilic attacks, where the color scale ranges from blue (electron deficiency centers) to red (electron-rich centers). The electrostatic potential values on the surface of the system can also translate the electronic behavior.

In the case of the Cr-complex, the potential appears to be equally distributed on the surface of the complex, with a slightly negative area located around the phenyl moieties. The blue color is surrounded by the coordination sphere due to the presence of hydrogen atoms of coordinated water. Similarly, in the case of the Ru-complex, the positive site appears near the coordination sphere mainly due to the presence of H-atoms or

coordinated water. This point is encouraged by the presence of a shorter M-O_1 bond length compared to the Fe-complex.

For the Fe-complex, slightly more negative charges are found around the phenyl parts besides the electron-rich coordination sphere. This is due to further interactions between (LH_2) donor sites and the metal center.

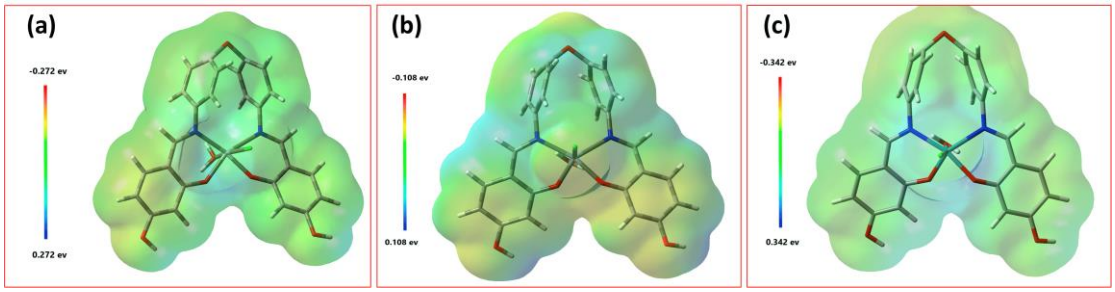

Figure 9: Molecular electrostatic potential map of the (TVMC)s of (a) Cr(III), (b) Fe(III), and (c) Ru(III)

Electron Localization Function (ELF)

The identification of electron localization areas on the surface of metal complexes is a crucial step in understanding their electronic behavior. To achieve this, the ELF (Electron Localization Function) method is often used, which describes the localized electron-rich sites surrounding the metal center. In this study, the equatorial planes of the coordinated area were analyzed for the three complexes (TVMC), including Cr-complex, Fe-complex, and Ru-complex. The four equatorial coordinated atoms (N_1-M-O_2, N_1-M-O_3, N_2-M-O_2, and N_2-M-O_3) were examined to predict the electronic behavior in this region, as depicted in **Figures 10-12**.

The analysis of the ELF deformation map indicated the presence of mostly red color around the coordinated atoms, especially around N atoms with a localized direction towards the metal center, indicating a direct N-contact in plane with the metal center. Conversely, the deformation map appeared mostly around O-coordinated atoms, indicating a slight distortion of O atoms from the metal plane. This difference in electronic distribution can be attributed to the electron donor ability of N atoms over O atoms. Additionally, the electronic red map around the central metal was used to detect potentially interactions with donor atoms.

Regarding the Fe-complex, the equatorial map showed localized electron spots or domains directed toward each coordinate bond, unlike the other complexes, which may affect the strength of the interaction between the active centers. Overall, the ELF method provided valuable insights into the electron localization areas and electronic behavior of the studied metal complexes.

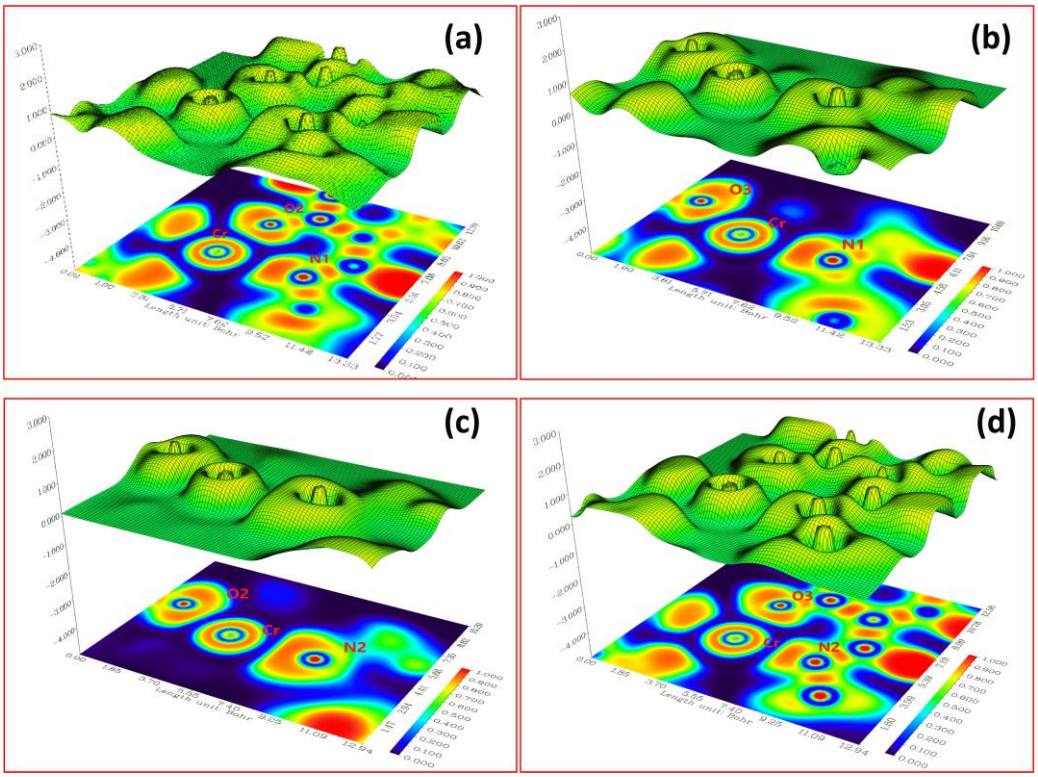

Figure 10: Shaded surface map with projection for ELF of Cr(III)-complex with planes (a) N_1CrO_2, (b) N_1CrO_3, (c) N_2CrO_2, (d) N_2CrO_3

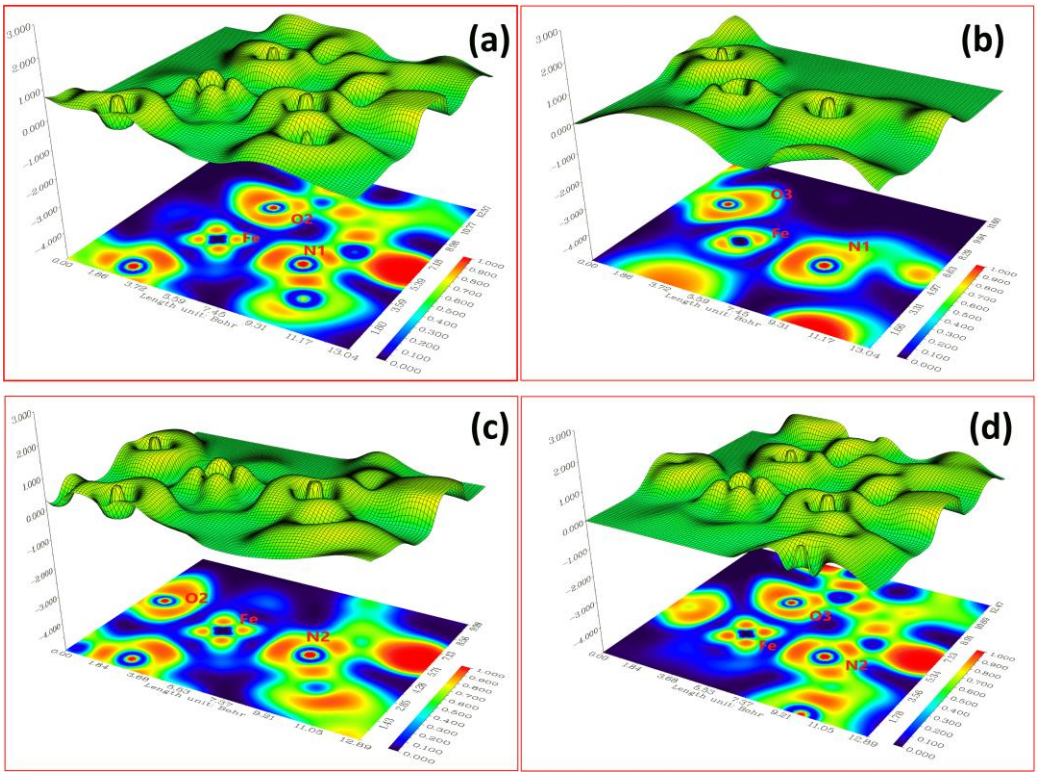

Figure 11: Shaded surface map with projection for ELF of Fe(III)-complex with planes (a) N_1FeO_2, (b) N_1FeO_3, (c) N_2FeO_2, (d) N_2FeO_3

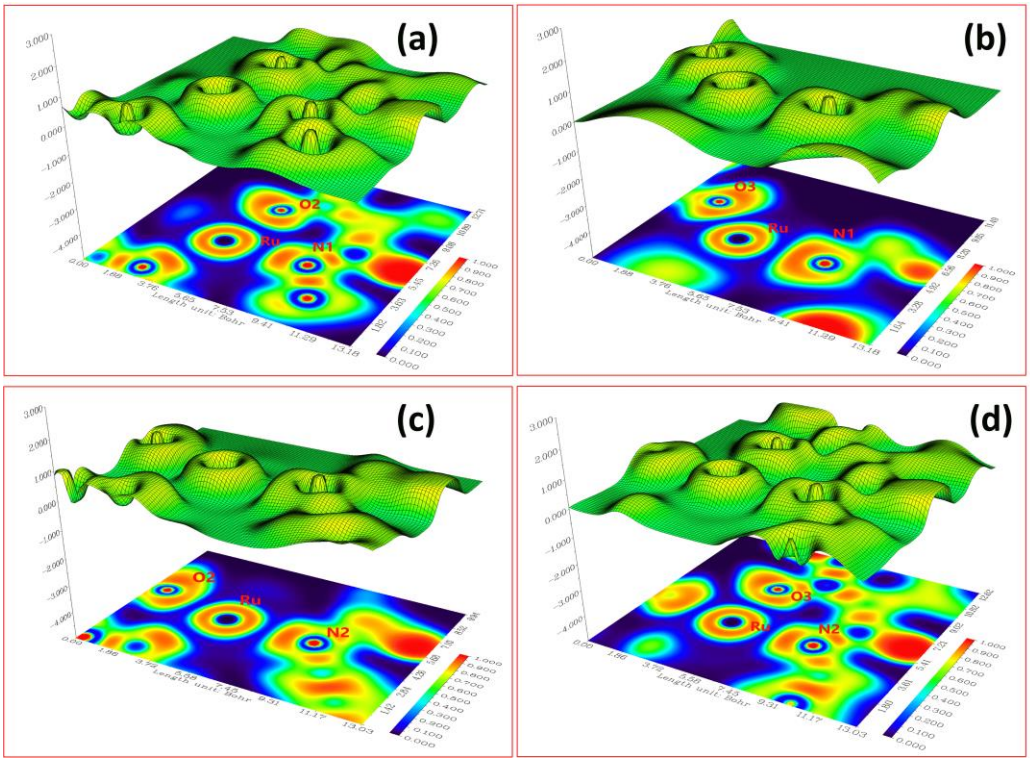

Figure 12: Shaded surface map with projection of ELF of Ru(III)-complex with planes (a) N_1RuO_2, (b) N_1RuO_3, (c) N_2RuO_2, (d) N_2RuO_3

Computational IR spectra

The computational vibrational harmonic spectra with corrected scale factors were listed in **Table 8** for comparison with experimental data. **Figure 13** gives the computational DFT-IR spectra for the synthesized (TVMC)s.

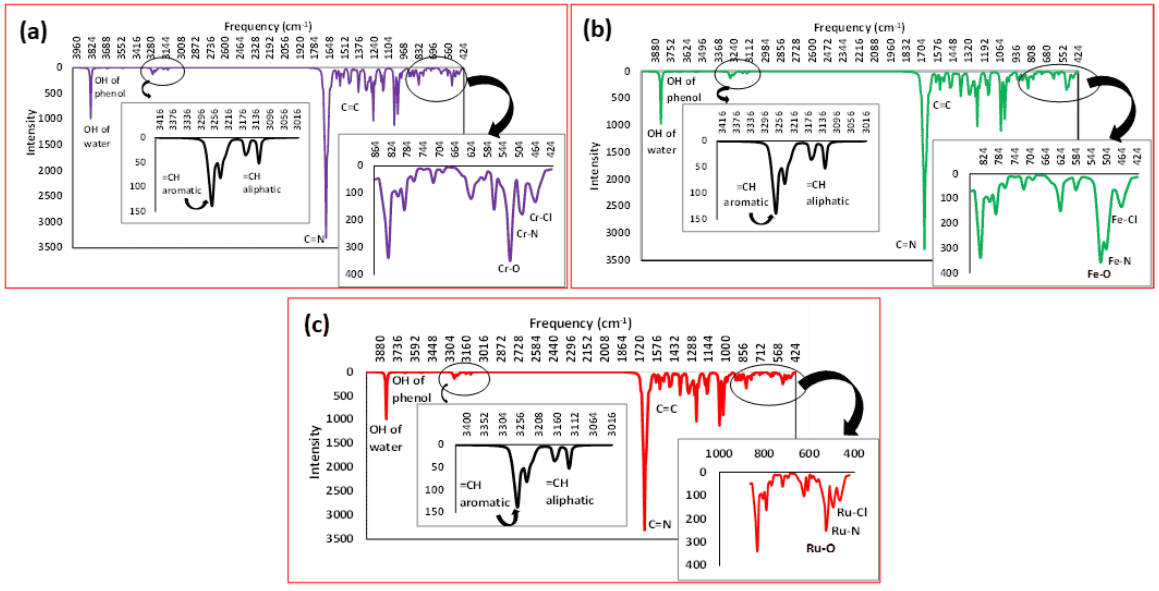

Figure 13: Computational IR spectra of the complexes (a) Cr(III), (b) Fe(III), and (c) Ru(III) With enlarged spectral area from 3000 to 3050 cm^{-1} and from 400 to 800 cm^{-1}

Table 8: Calculated frequencies of B3LYP/6-311G(d,p) and experimental IR frequencies.

Functional group	FrequencyB3LYP/ 6-311G(d,p)(cm^{-1})	Frequency x scale Factor(cm^{-1})	Experimental Frequency(cm^{-1})
Cr-complex			
OH (Phenol)	3780	3655	3238
O-H (coordinate-water)	3540-3670	3423-3548	3367
=C-H (aromatic)	3220-3277	3113-3168	3053
=C-H (aliphatic)	3127-3164	3023-3059	2888
C=N	1680	1624	1608
C=C	1518-1623	1467-1569	1497
C-O	1384	1338	1244
Cr-O	528	507	555
Cr-N	496	476	484
Cr-Cl	464	446	456
Fe-complex			
OH (Phenol)	3780	3655	3237
O-H (coordinate-water)	3540-3670	3423-3548	3346
=C-H (aromatic)	3220-3277	3113-3168	3067
=C-H (aliphatic)	3127-3164	3023-3059	2956
C=N	1680	1624	1606
C=C	1518-1623	1467-1569	1501
C-O	1384	1338	1240
Fe-O	520	499	529
Fe-N	504	484	488
Fe-Cl	464	446	419
Ru-complex			
OH (Phenol)	3780	3655	3240
O-H (coordinate-water)	3540-3670	3423-3548	3445
=C-H (aromatic)	3220-3277	3113-3168	3069
=C-H (aliphatic)	3127-3164	3023-3059	2882
C=N	1680	1624	1638
C=C	1518-1623	1467-1569	1492
C-O	1384	1338	1241
Ru-O	530	509	536
Ru-N	496	476	490
Ru-Cl	472	453	458

The results presented in the computational study provide information about the geometrical properties and electronic behavior of metal complexes (TVMC) containing chelating (LH_2) ligands. The angle values and bond lengths presented in **Table 6** indicate that (LH_2) active sites play a significant role in the distortion of the complexes' geometrical configuration, resulting in different bond angles and bond lengths. The quantum chemical reactivity parameters presented in **Table 7**, such as electronegativity, ionization potential, electron affinity, chemical potential, chemical hardness, and global softness, provide insights into the electronic properties and stability of the studied complexes. The FMO analysis indicates that the studied complexes have large electronic distribution scales, leading to the formation of highly stable complexes. The MEP analysis and ELF method were used to identify electrophilic and nucleophilic attacks and localize electron-

rich sites surrounding the metal center. Overall, the results provide valuable insights into the properties of metal complexes and their electronic behavior, which can aid in the design and development of new metal-based compounds with improved properties.

Antibacterial activity

The primary objective of any antibacterial agent is to impede the growth of harmful bacteria without exhibiting any harmful effects on the host organism[28]. In order to evaluate the antibacterial properties of the Schiff base ligand (LH_2) and its (TVMC)s, two microorganisms (*Staphylococcus aureus* (+v) and *Escherichia coli* (-ve)) were chosen. The antibacterial activities of (LH_2) and its metal complexes were compared with those of the standard antibiotic Cefotaxime (CTX-30).

Table 9 displays the results obtained from the antibacterial activity tests conducted using *Staphylococcus aureus* a (+v) and *Escherichia coli* (-ve) as test organisms. DMSO was used as a negative control and was found to have no antibacterial activity against the tested bacteria. In fact, the metal complexes of the ligands usually have higher biological activity than the ligands themselves[77–80]. The data indicates that (TVMC)s are more effective in inhibiting the growth of microorganisms compared to the Schiff base (LH_2), except for the Ru(III) and Cr(III) complexes which did not exhibit any antibacterial activity against *S. aureus* and *E. coli*. The Fe(III) complex was the most effective antibacterial agent among the ligand and its metal complexes, showing an inhibitory zone of 15 mm for *E. coli* and 13 mm for *S. aureus*. This indicates that the complexes are more effective than the parent (LH_2) compound which did not exhibit activity against any of the tested bacteria. However, the antibacterial activity of (LH_2) and its complexes was lower than that of the standard Cefotaxime (CTX-30). The size of the inhibition zone was found to depend on various factors such as culture medium, incubation conditions, rate of diffusion, and the concentration of the antibacterial agent.

The observed activities of the tested complexes can be explained by the chelation theory. Chelation reduces the polarity of the metal atom by sharing its positive charge with the donor groups, and potential p-electron delocalization within the entire chelate ring enhances the lipophilicity of the complex. This increase in lipophilicity facilitates the passage of the complex across the lipid layer of the cell membrane[28, 81, 82].

This study's significance is rooted in the potential application of these complexes in the treatment of prevalent diseases such as septicemia, gastroenteritis, urinary tract infections, and hospital-acquired infections, caused by *Escherichia coli*[83].

Table 9: Antibacterial activity data of (LH_2) and their (TVMC)s

Compounds	Inhibition Zone (mm)	
	Escherichia coli **Gram(-)**	***Staphylococcus Aureus*** **Gram(+)**
Ligand (LH_2)	-	-
$[Fe(L)(Cl)(H_2O)].3H_2O$	15	13
$[Cr(L)(Cl)(H_2O)].3H_2O$	-	-
$[Ru(L)(Cl)(H_2O)].2H_2O$	-	-
CTX-30	25	25
Control: DMSO	-	-

Conclusions

In this study, we prepared and characterized three novel complexes of Ru(III), Cr(III), and Fe(III) based on a symmetrical Schiff base (LH_2) for the first time. The complexes were characterized using analytical and spectroscopic techniques, which revealed that (LH_2) coordinates with the central transition metal ions in a tetradentate way through two azomethine nitrogen atoms (CH=N) and two phenolic oxygens (–OH) in a 1:1 (M:L) molar ratio and all complexes have an octahedral shape. DFT calculations confirmed the octahedral shape of the complexes and revealed their geometrical and electronic properties. The ligands' active sites influenced the complexes' structure and stability, which were also analyzed by quantum chemical and FMO methods.

The complexes are thermally stable up to 138°C and decompose in several steps. The decomposition of the complexes involved several steps, with chelating ligands exhibiting higher thermal stability compared to non-chelating ligands. The chelating ligands, the water molecules, and the metal oxides support the structure. Our findings can be useful in the development of new metal-based compounds with enhanced properties. Furthermore, we studied the antibacterial activity of the ligand and the complexes against *E. coli* and *S. aureus* in vitro. Only the Fe(III) complex showed activity against both bacteria. In conclusion, our findings reveal the coordination chemistry and antibacterial properties of these new metal complexes, which may be useful for treating *E. coli* infections. For future work on these complexes, it is suggested to explore their potential applications in various fields beyond the scope of this study.

Data Availability

The data used to support the findings of this study are available at the Department of Chemistry, College of Science, the University of Sulaimani.

Conflict of interest

The authors confirm that they are not affiliated with or involved in any organization or entity with financial interests.

Acknowledgments

The authors gratefully acknowledge the support for this study from the University of Sulaimani, University of Garmian, and University of Human Development

Author Contributions

Conceptualization, Hanar Q. Hassan, Karzan Abdalkarim, Dalia A. Abdul, Diary I. Tofiq, Rebaz Hamarawf and Shujahadeen B. Aziz; Data curation, Aso Hasan Hameed; Formal analysis, Hanar Q. Hassan, Aso Hasan Hameed and Rebaz Hamarawf ; Funding acquisition, Dalia A. Abdul and Diary I. Tofiq; Investigation, Hanar Q. Hassan, Karzan Abdalkarim and Rebaz Hamarawf ; Methodology, Hanar Q. Hassan, Karzan Abdalkarim and Rebaz Hamarawf ; Project administration, Dalia A. Abdul, Aso Hasan Hameed, Diary I. Tofiq, Rebaz Hamarawf and Shujahadeen B. Aziz; Supervision, Diary I. Tofiq; Validation, Karzan Abdalkarim, Dalia A. Abdul, Aso Hasan Hameed, Diary I. Tofiq, Rebaz Hamarawf and Shujahadeen B. Aziz; Visualization, Aso Hasan Hameed; Writing – original draft, Hanar Q. Hassan and Karzan Abdalkarim; Writing – review & editing, Dalia A. Abdul, Aso Hasan Hameed, Diary I. Tofiq, Rebaz Hamarawf , Kawan F. Kayani and Shujahadeen B. Aziz.

References

1. K. A. Abdalkarim et al., (2021,). 'Synthesis of Hg metal complex and its application to reduce the optical band gap of polymer', Arab. J. Chem., vol. 14, no. 7, p. 103215, doi: 10.1016/j.arabjc.2021.103215.
2. B. Murukan and K. Mohanan, (2007). 'Synthesis, characterization and antibacterial properties of some trivalent metal complexes with [(2-hydroxyl-1-naphthaldehyde)-3-isatin]-bishydrazone', J. Enzyme Inhib.

Med. Chem., vol. 22, no. 1, pp. 65–70, doi: 10.1080/14756360601027373.
3. Z. A. Taha et al., (2012). 'Structural, luminescence and biological studies of trivalent lanthanide complexes with N,N′-bis(2-hydroxynaphthylmethylidene)-1,3-propanediamine Schiff base ligand', J. Lumin., vol. 132, no. 11, pp. 2832–2841, doi: 10.1016/j.jlumin.2012.05.041.
4. H. Kargar et al., (2022). 'Spectroscopic investigation, molecular structure, catalytic activity with computational studies of a novel Pd(II) complex incorporating unsymmetrical tetradentate Schiff base ligand', Inorg. Chem. Commun., vol. 142, p. 109697, doi: https://doi.org/10.1016/j.inoche.2022.109697.
5. S. H. Sumrra et al., (2021). 'Metal incorporated aminothiazole-derived compounds: Synthesis, density function theory analysis, in vitro antibacterial and antioxidant evaluation', R. Soc. Open Sci., vol. 8, no. 9, doi: 10.1098/rsos.210910.
6. M. A. Malik et al., (2018). 'Heterocyclic Schiff base transition metal complexes in antimicrobial and anticancer chemotherapy', Medchemcomm, vol. 9, no. 3, pp. 409–436, doi: 10.1039/c7md00526a.
7. V. Ritleng et al., (2016). 'Nickel N-Heterocyclic Carbene-Catalyzed C-Heteroatom Bond Formation, Reduction, and Oxidation: Reactions and Mechanistic Aspects', ACS Catal., vol. 6, no. 2, pp. 890–906, doi: 10.1021/acscatal.5b02021.
8. Y. Liu et al., (2017). 'Inorganic anion-dependent assembly of zero-, one-, two- and three-dimensional Cu(II)/Ag(I) complexes under the guidance of the HSAB theory: Synthesis, structure, and magnetic property', J. Solid State Chem., vol. 246, no. November 2016, pp. 48–56, doi: 10.1016/j.jssc.2016.10.030.
9. R. G. Pearson, (1963). 'Hard and Soft Acids and Bases', J. Am. Chem. Soc., vol. 85, no. 22, pp. 3533–3539, doi: 10.1021/ja00905a001.
10. R. D. Hancock and A. E. Martell, (1996). 'Hard and soft acid-base behavior in aqueous solution: Steric effects make some metal ions hard a quantitative scale of hardness-softness for acids and bases', Journal of Chemical Education, vol. 73, no. 7. pp. 654–661, doi: 10.1021/ed073p654.
11. E. Langer et al., (2019). 'Application of new modified Schiff base epoxy resins as organic coatings', J. Coatings Technol. Res., vol. 16, no. 4, pp. 1109–1120, doi: 10.1007/s11998-019-00185-7.
12. M. Murmu et al., (2019). 'Amine cured double Schiff base epoxy as efficient anticorrosive coating materials for protection of mild steel in 3.5% NaCl medium', J. Mol. Liq., vol. 278, pp. 521–535, doi: 10.1016/j.molliq.2019.01.066.
13. K. Wang et al., (2022). 'Iron complexes of [2+2] and [6+6] Schiff-base macrocycles derived from 2,2′-oxydianiline and their applications', Inorg. Chem. Commun., vol. 139, no. January, p. 109376, doi: 10.1016/j.inoche.2022.109376.
14. C. Redshaw, (2017). 'Use of metal catalysts bearing schiff base macrocycles for the ring opening polymerization (ROP) of cyclic esters', Catalysts, vol. 7, no. 5, doi: 10.3390/catal7050165.
15. W. Yang et al., (2016). 'Structural studies of Schiff-base [2 + 2] macrocycles derived from 2,2′-oxydianiline and the ROP capability of their organoaluminium complexes', Dalt. Trans., vol. 45, no. 30, pp. 11990–12005, doi: 10.1039/c6dt01997h.
16. R. Muthusami et al., (2021). 'Cu(II) Schiff base complex functionalized mesoporous silica nanoparticles as an efficient catalyst for the synthesis of questiomycin A and photo-Fenton-like rhodamine B degradation', J. Solid State Chem., vol. 302, no. July, p. 122429, doi: 10.1016/j.jssc.2021.122429.
17. Z. Uyar et al., (2017). 'Synthesis, Characterization, and Cytotoxic Activities of a Schiff Base Ligand and Its Binuclear Copper(II) and Manganese(III) Complexes', J. Turkish Chem. Soc. Sect. A Chem., vol. 4, no. 3, pp. 963–980, doi: 10.18596/jotcsa.329108.
18. H. Keypour et al., (2013). 'Synthesis, spectral characterization, structural investigation and antimicrobial studies of mononuclear Cu(II), Ni(II), Co(II), Zn(II) and Cd(II) complexes of a new potentially hexadentate N2O4 Schiff base ligand derived from salicylaldehyde', J. Mol. Struct., vol. 1032, pp. 62–68, doi: 10.1016/j.molstruc.2012.07.056.
19. G. Kumar et al., (2010). 'Synthesis, physical characterization and antimicrobial activity of trivalent metal Schiff base complexes', J. Serbian Chem. Soc., vol. 75, no. 5, pp. 629–637, doi: 10.2298/JSC090704037K.
20. A. Fatoni et al., (2018). 'Synthesis and characterization of chitosan linked by methylene bridge and schiff base of 4,4-diaminodiphenyl ether-vanillin', Indones. J. Chem., vol. 18, no. 1, pp. 92–101, doi: 10.22146/ijc.25866.
21. A. A. Jarrahpour and M. Zarei, (2004). 'Synthesis of 2-({[4-(4-{[(E)-1-(2-hydroxy-3-methoxyphenyl) methylidene]amino}phenoxy)phenyl]imino}methyl)- 6 -methoxy phenol', Molbank, vol. 87, no. M352, pp. 2003–2004,
22. E. Langer et al., (2019). 'Application of new modified Schiff base epoxy resins as organic coatings', J. Coatings Technol. Res., vol. 16, no. 4, pp. 1109–1120, doi: 10.1007/s11998-019-00185-7.

23. E. Langer et al., (2014). 'Self-stratifying coatings based on Schiff base epoxy resins', J. Coatings Technol. Res., vol. 11, no. 6, pp. 865–872, doi: 10.1007/s11998-014-9603-x.
24. M. Salavati-Niasari and M. Bazarganipour, (2007). 'Effect of single-wall carbon nanotubes on direct epoxidation of cyclohexene catalyzed by new derivatives of cis-dioxomolybdenum(VI) complexes with bis-bidentate Schiff-base containing aromatic nitrogen-nitrogen linkers', J. Mol. Catal. A Chem., vol. 278, no. 1–2, pp. 173–180, doi: 10.1016/j.molcata.2007.09.009.
25. Z. Parsaee and K. Mohammadi, (2017). 'Synthesis, characterization, nano-sized binuclear nickel complexes, DFT calculations and antibacterial evaluation of new macrocyclic Schiff base compounds', J. Mol. Struct., vol. 1137, pp. 512–523, doi: 10.1016/j.molstruc.2017.02.026.
26. A. A. Nazarov et al., (2014). 'Opening the lid on piano-stool complexes: An account of ruthenium(II)earene complexes with medicinal applications', J. Organomet. Chem., vol. 751, pp. 251–260, doi: 10.1016/j.jorganchem.2013.09.016.
27. P. V. Anantha Lakshmi et al., (2008). 'Synthesis and structural studies of first row transition metal complexes of n-(2-nitro)-benzilidine-3-hydrazino quinoxaline-2-one', Bull. Chem. Soc. Ethiop., vol. 22, no. 3, pp. 385–390, doi: 10.4314/bcse.v22i3.61215.
28. W. H. Mahmoud et al (2016). 'Novel Schiff base ligand and its metal complexes with some transition elements. Synthesis, spectroscopic, thermal analysis, antimicrobial and in vitro anticancer activity', Appl. Organomet. Chem., vol. 30, no. 4, pp. 221–230, doi: 10.1002/aoc.3420.
29. A. Singh and P. Barman, (2021). Recent Advances in Schiff Base Ruthenium Metal Complexes: Synthesis and Applications, vol. 379, no. 4. Springer International Publishing.
30. A. Çapan et al (2018). 'Ru(III), Cr(III), Fe(III) complexes of Schiff base ligands bearing phenoxy Groups: Application as catalysts in the synthesis of vitamin K3', J. Saudi Chem. Soc., vol. 22, no. 6, pp. 757–766, doi: 10.1016/j.jscs.2017.12.007.
31. J. Patole et al (2006). 'Schiff base conjugates of p-aminosalicylic acid as antimycobacterial agents', Bioorganic Med. Chem. Lett., vol. 16, no. 6, pp. 1514–1517, doi: 10.1016/j.bmcl.2005.12.035.
32. Y. Lu et al (2012). 'Synthesis, structures, and urease inhibition of nickel(II), zinc(II), and cobalt(II) complexes with similar hydroxy-rich Schiff bases', J. Coord. Chem., vol. 65, no. 2, pp. 339–352, doi: 10.1080/00958972.2011.653785.
33. S. K. Dey and A. Mukherjee, (2014). 'The synthesis, characterization and catecholase activity of dinuclear cobalt(ii/iii) complexes of an O-donor rich Schiff base ligand', New J. Chem., vol. 38, no. 10, pp. 4985–4995, doi: 10.1039/c4nj00715h.
34. A. Banerjee and S. Chattopadhyay, (2019). 'Synthesis and characterization of mixed valence cobalt(III)/cobalt(II) complexes with N,O-donor Schiff base ligands', Polyhedron, vol. 159, no. Iii, pp. 1–11, doi: 10.1016/j.poly.2018.10.059.
35. P. P. Yang et al (2010). 'Syntheses, crystal structures and magnetic properties of a novel family of penta-manganese complexes derived from an assembly system containing polydentate hydroxy-rich Schiff-base ligands', Dalt. Trans., vol. 39, no. 27, pp. 6285–6294, doi: 10.1039/c0dt00291g.
36. C. Garino and L. Salassa, (2013). 'The photochemistry of transition metal complexes using density functional theory', Philos. Trans. R. Soc. A, vol. 371, no. 1995, doi: 10.1098/rsta.2012.0134.
37. S. Noreen and S. H. Sumrra, (2021). 'Aminothiazole-Linked Metal Chelates: Synthesis, Density Functional Theory, and Antimicrobial Studies with Antioxidant Correlations', ACS Omega, vol. 6, no. 48, pp. 33085–33099, doi: 10.1021/acsomega.1c05290.
38. A. U. Hassan et al., (2022). 'New organosulfur metallic compounds as potent drugs: synthesis, molecular modeling, spectral, antimicrobial, drug likeness and DFT analysis', Mol. Divers., vol. 26, no. 1, pp. 51–72, doi: 10.1007/s11030-020-10157-4.
39. S. C. Qi et al (2010). 'Application of Density Functional Theory in the Calculations Involving Metal Complexes', RSC Adv., vol. 6, no. 81, pp. 77375–77395, 2016, doi: 10.1039/c6ra16168e.
40. M. J. Frisch et al., 'Gaussian 09, Revision B.01'. Gaussian Inc., Wallingford.
41. Shehnaz, W. A. et al., (2023). 'Sulfonamide derived Schiff base Mn (II), Co (II), and Ni (II) complexes: Crystal structures, density functional theory and Hirshfeld surface analysis', Appl. Organomet. Chem., vol. 37, no. 6, p. e7077, Jun. doi: https://doi.org/10.1002/aoc.7077.
42. H. Kargar et al., (2022). 'Synthesis, crystal structure, spectral characterization, catalytic studies and computational studies of Ni(II) and Pd(II) complexes of symmetrical tetradentate Schiff base ligand', J. Coord. Chem., vol. 75, no. 7–8, pp. 972–993, Apr. doi: 10.1080/00958972.2022.2092846.
43. R. H. H. Salih et al., (2023). 'Thiazole-pyrazoline hybrids as potential antimicrobial agent: Synthesis, biological evaluation, molecular docking, DFT studies and POM analysis', J. Mol. Struct., vol. 1282, p.

135191, doi: https://doi.org/10.1016/j.molstruc.2023.135191.
44. K. Anbukarasi et al., (2023). 'DFT and Molecular Docking Analysis of Newly Synthesized Compound (2E)-3-[3-(Benzyloxy) Phenyl]-1-(4'-Chlorophe-Nyl)-2-Propen-1-One [Bpclpo]', Current Physical Chemistry, vol. 13. pp. 1–38, doi: http://dx.doi.org/10.2174/1877946812666220928102954.
45. D. S. E. Sayed and E. S. M. Abdelrehim, (2022). 'Spectroscopic details on the molecular structure of pyrimidine-2-thiones heterocyclic compounds: computational and antiviral activity against the main protease enzyme of SARS-CoV-2', BMC Chem., vol. 16, no. 1, pp. 1–18, doi: 10.1186/s13065-022-00881-3.
46. S. Chiodo, et al., (2006). 'LANL2DZ basis sets recontracted in the framework of density functional theory', J. Chem. Phys., vol. 125, no. 10, doi: 10.1063/1.2345197.
47. Y. Yang et al., (2009). 'Assessment of the "6-31+Gt; + LANL2DZ" mixed basis set coupled with density functional theory methods and the effective core potential: Prediction of heats of formation and ionization potentials for first-row-transition-metal complexes', J. Phys. Chem. A, vol. 113, no. 36, pp. 9843–9851, doi: 10.1021/jp807643p.
48. L. E. Roy et al., (2008). 'Revised basis sets for the LANL effective core potentials', J. Chem. Theory Comput., vol. 4, no. 7, pp. 1029–1031, doi: 10.1021/ct8000409.
49. Semenov, 'Chemcraft'. 2021, [Online]. Available: https://www.chemcraftprog.com/.
50. 'GaussView, Version 6.1, Roy Dennington, Todd A. Keith, and John M. Millam, Semichem Inc., Shawnee Mission, KS, 2016.' [Online]. Available: https://www.scirp.org/(S(351jmbntvnsjt1aadkposzje))/reference/referencespapers.aspx?referenceid=2130491
51. R. H. H. Salih et al., (2022). 'One-pot synthesis, molecular docking, ADMET, and DFT studies of novel pyrazolines as promising SARS-CoV-2 main protease inhibitors', Res. Chem. Intermed., vol. 48, no. 11, pp. 4729–4751, doi: 10.1007/s11164-022-04831-5.
52. G. Serdaroğlu et al., (2021). 'Carbazole derivatives: Synthesis, spectroscopic characterization, antioxidant activity, molecular docking study, and the quantum chemical calculations', J. Mol. Liq., vol. 330, doi: 10.1016/j.molliq.2021.115651.
53. 'https://cccbdb.nist.gov/vibscalejust.asp'. https://cccbdb.nist.gov/vibscalejust.asp.
54. T. Lu and F. Chen, (2012). 'Multiwfn: A multifunctional wavefunction analyzer', J. Comput. Chem., vol. 33, no. 5, pp. 580–592, doi: 10.1002/jcc.22885.
55. T. A. Alorini et al., (2022). 'Synthesis, characterization, and anticancer activity of some metal complexes with a new Schiff base ligand', Arab. J. Chem., vol. 15, no. 2, p. 103559, doi: 10.1016/j.arabjc.2021.103559.
56. C. Ding et al., (2013). 'Polynuclear complexes with alkoxo and phenoxo bridges from in situ generated hydroxy-rich Schiff base ligands: Syntheses, structures, and magnetic properties', Chem. - A Eur. J., vol. 19, no. 30, pp. 9961–9972, doi: 10.1002/chem.201301041.
57. D. I. Tofiq, et al., (2021). 'Preparation of a novel Mixed-Ligand divalent metal complexes from solvent free Synthesized Schiff base derived from 2,6-Diaminopyridine with cinnamaldehyde and 2,2′-Bipyridine: Characterization and antibacterial activities', Arab. J. Chem., vol. 14, no. 12, p. 103429, doi: 10.1016/j.arabjc.2021.103429.
58. B. M. Kukovec et al., (2008). 'Synthesis and structure of cobalt(II) complexes with hydroxyl derivatives of pyridinecarboxylic acids: Conformation analysis of ligands in the solid state', J. Mol. Struct., vol. 882, no. 1–3, pp. 47–55, doi: 10.1016/j.molstruc.2007.09.011.
59. S. A. Aboafia et al., (2018). 'New transition metal complexes of 2,4-dihydroxybenzaldehyde benzoylhydrazone Schiff base (H2dhbh): Synthesis, spectroscopic characterization, DNA binding/cleavage and antioxidant activity', J. Mol. Struct., vol. 1158, pp. 39–50, doi: 10.1016/j.molstruc.2018.01.008.
60. R. Takjoo et al., 'Co(III) and Fe(III) complexes of Schiff bases derived from 2,4-dihydroxybenzaldehyde S-allyl-isothiosemicarbazonehydrobromide', J. Coord. Chem., vol. 66, no. 22, pp. 3915–3925, 2013, doi: 10.1080/00958972.2013.856420.
61. Y. Lu, et al., (2012). 'Synthesis, structures, and urease inhibition of nickel(II), zinc(II), and cobalt(II) complexes with similar hydroxy-rich Schiff bases', J. Coord. Chem., vol. 65, no. 2, pp. 339–352, doi: 10.1080/00958972.2011.653785.
62. A. C. Ekennia et al., (2015). 'Synthesis, DFT Calculation, and Antimicrobial Studies of Novel Zn(II), Co(II), Cu(II), and Mn(II) Heteroleptic Complexes Containing Benzoylacetone and Dithiocarbamate', Bioinorg. Chem. Appl., vol. 2015, pp. 1–12, doi: 10.1155/2015/789063.
63. K. A. Abdalkarim et al., (2021). 'Synthesis of Hg metal complex and its application to reduce the optical band gap of polymer', Arab. J. Chem., vol. 14, no. 7, p. 103215, doi: 10.1016/j.arabjc.2021.103215.
64. S. Dutta Gupta et al., (2015). '2,4-dihydroxy benzaldehyde derived Schiff bases as small molecule Hsp90 inhibitors: Rational identification of a new anticancer lead', Bioorg. Chem., vol. 59, pp. 97–105, doi:

10.1016/j.bioorg.2015.02.003.
65. S. Shaygan, et al., (2018). 'Cobalt (II) complexes with Schiffbase ligands derived from terephthalaldehyde and ortho-substituted anilines: Synthesis, characterization and antibacterial activity', Appl. Sci., vol. 8, no. 3, doi: 10.3390/app8030385.
66. A. S. Alturiqi et al., (2018). 'Synthesis, Spectral Characterization, and Thermal and Cytotoxicity Studies of Cr(III), Ru(III), Mn(II), Co(II), Ni(II), Cu(II), and Zn(II) Complexes of Schiff Base Derived from 5-Hydroxymethylfuran-2-carbaldehyde', J. Chem., vol. 2018, doi: 10.1155/2018/5816906.
67. M. Mohamed Subarkhan and R. Ramesh, (2015). 'Binuclear ruthenium(III) bis(thiosemicarbazone) complexes: Synthesis, spectral, electrochemical studies and catalytic oxidation of alcohol', Spectrochim. Acta - Part A Mol. Biomol. Spectrosc., vol. 138, no. Iii, pp. 264–270, doi: 10.1016/j.saa.2014.11.039.
68. L. A. Saghatforoush et al., (2009). 'Iron(III) Schiff base complexes with asymmetric tetradentate ligands: Synthesis, spectroscopy, and antimicrobial properties', Transit. Met. Chem., vol. 34, no. 8, pp. 899–904, doi: 10.1007/s11243-009-9279-8.
69. A. N. E. and Y. Z. A. A.M. Nassar*, A.M. Hassan, (2012). 'Synthesis and characterization of novel binuclear complexes', Int. J. Chem. Biochem. Sci., vol. 2, pp. 83–93.
70. J. T. P. Matshwele et al., (2020). 'Synthesis of Mixed Ligand Ruthenium (II/III) Complexes and Their Antibacterial Evaluation on Drug-Resistant Bacterial Organisms', J. Chem., vol. 2020, doi: 10.1155/2020/2150419.
71. J. Joseph et al., (2013). 'Synthesis, characterization and antimicrobial activities of copper complexes derived from 4-aminoantipyrine derivatives', J. Saudi Chem. Soc., vol. 17, no. 3, pp. 285–294, doi: 10.1016/j.jscs.2011.04.007.
72 A. Palanimurugan et al., (2019). 'Electrochemical behavior, structural, morphological, Calf Thymus-DNA interaction and in-vitro antimicrobial studies of synthesized Schiff base transition metal complexes', Heliyon, vol. 5, no. 7, p. e02039, doi: 10.1016/j.heliyon.2019.e02039.
73. B. A. Ismail et al., (2021). 'Synthesis, characterization, thermal, DFT computational studies and anticancer activity of furfural-type schiff base complexes', J. Mol. Struct., vol. 1227, p. 129393, doi: https://doi.org/10.1016/j.molstruc.2020.129393.
74. S. F. A. Kettle, (2021). 'Stability of coordination compounds', in Physical Inorganic Chemistry, 1996, pp. 73–94.
75. N. Al-Zaqri et al., 'Structural investigations, quantum mechanical studies on proton and metal affinity and biological activity predictions of selpercatinib', J. Mol. Liq., vol. 325, p. 114765, doi: 10.1016/j.molliq.2020.114765.
76. P. Geerlings and F. De Proft, (2002). 'Chemical reactivity as described by quantum chemical methods', Int. J. Mol. Sci., vol. 3, no. 4, pp. 276–309, doi: 10.3390/i3040276.
77. S. H. Sumrra et al., (2022). 'Metal incorporated sulfonamides as promising multidrug targets: Combined enzyme inhibitory, antimicrobial, antioxidant and theoretical exploration', J. Mol. Struct., vol. 1250, p. 131710, doi: https://doi.org/10.1016/j.molstruc.2021.131710.
78. G. Mustafa et al., (2022). 'A critical review on recent trends on pharmacological applications of pyrazolone endowed derivatives', J. Mol. Struct., vol. 1262, p. 133044, doi: https://doi.org/10.1016/j.molstruc.2022.133044.
79. S. H. Sumrra et al., (2022). 'A review on the biomedical efficacy of transition metal triazole compounds', J. Coord. Chem., vol. 75, no. 3–4, pp. 293–334, Feb. doi: 10.1080/00958972.2022.2059359.
80. A. U. Hassan et al., (2021). 'Design, facile synthesis, spectroscopic characterization, and medicinal probing of metal-based new sulfonamide drugs: A theoretical and spectral study', Appl. Organomet. Chem., vol. 35, no. 1, pp. 1–17, doi: 10.1002/aoc.6054.
81. F. N. Sayed et al., (2023). 'Structural characterization and molecular docking studies of biologically active platinum(II) and palladium(II) complexes of ferrocenyl Schiff bases', J. Mol. Struct., vol. 1278, p. 134904, doi: 10.1016/j.molstruc.2023.134904.
82. Y. A. A. Alghuwainem et al., (2023). 'Synthesis, structural, DFT, antibacterial, antifungal, anti-inflammatory, and molecular docking analysis of new VO(II), Fe(III), Mn(II), Zn(II), and Ag(I) complexes based on 4-((2-hydroxy-1-naphthyl)azo) benzenesulfonamide', J. Mol. Liq., vol. 369, p. 120936, doi: 10.1016/j.molliq.2022.120936.
83. M. H. Soliman and G. G. Mohamed, (2012). 'Preparation, spectroscopic and thermal characterization of new metal complexes of verlipride drug. in vitro biological activity studies', Spectrochim. Acta - Part A Mol. Biomol. Spectrosc., vol. 91, pp. 11–17, doi: 10.1016/j.saa.2012.01.021.